Sensitivity of intracavity filtering schemes for detecting gravitational waves

Mengyao Wang,[1] Haixing Miao,[2] Andreas Freise,[1] and Yanbei Chen[2]

[1]*School of Physics and Astronomy, University of Birmingham, Birmingham B15 2TT, United Kingdom*
[2]*Theoretical Astrophysics 350-17, California Institute of Technology, Pasadena, California 91125, USA*

(Received 11 October 2013; published 31 March 2014)

We consider enhancing the sensitivity of future gravitational-wave detectors by adding optical filters inside the signal-recycling cavity—an intracavity filtering scheme, which coherently feeds the sideband signal back to the interferometer with a proper frequency-dependent phase. We study three cases of such a scheme with different motivations: (i) the case of backaction noise evasion, trying to cancel radiation-pressure noise with only one filter cavity for a signal-recycled interferometer; (ii) the speed-meter case, similar to the speed-meter scheme proposed by Purdue and Chen [Phys. Rev. D **66**, 122004 (2002)] but without the resonant-sideband-extraction mirror, and also relieves the optical requirement on the sloshing mirror; (iii) the broadband detection case with squeezed-light input, numerically optimized for a broadband sensitivity.

DOI: 10.1103/PhysRevD.89.062009 PACS numbers: 04.80.Nn, 95.55.Ym, 03.67.-a

I. INTRODUCTION

With advanced gravitational-wave (GW) detectors, such as Advanced LIGO [1] and Advanced VIRGO [2], now under construction, we will soon enter the stage in which the quantum noise, arising from vacuum fluctuation of the electromagnetic field, starts to play a significant role and sets the sensitivity limit over most of the detection band. The GW community has started a significant effort to develop techniques for quantum-noise reduction [3,4]. Such techniques generally include (i) modifying the input optics (input filtering), the use of frequency-dependent squeezing realized by using filter cavities to rotate the squeezing angle of the squeezed light in a frequency-dependent way, which enables a simultaneous reduction of the low-frequency radiation-pressure noise and the high-frequency shot noise; (ii) modifying the output optics (output filtering), the frequency-dependent readout by rotating the readout quadrature angle with filter cavities, which allows us to measure the proper quadrature and in turn cancel the radiation-pressure noise; (iii) coherently feeding the GW signals back to the interferometer, e.g., the signal-recycled Michelson [5] creating an optical spring that modifies the test mass dynamics, and the speed meter with a sloshing cavity [6] storing the earlier differential displacement information of the test masses to "slosh" it back to the interferometer with a negative sign or using an orthogonal polarized field to cancel the position information [7].

Here we consider a new scheme in which we place the optical filters inside the signal-recycling cavity, formed by the cavity input test masses (ITMs) and the signal-recycling mirror (SRM), and which we referred as an intracavity filtering scheme. Figure 1 schematically illustrates the configuration of a generic intracavity filtering scheme. The sideband fields are coherently fed back to the main interferometer. In some sense, this is one example of coherent feedback that has been extensively discussed in the quantum optics and control communities [8–11]. Depending on the choices of optical filters, different interferometer responses and sensitivities can be obtained. We will not exhaust all the possibilities, and only focus on the following three cases that have clear motivations.

Our first consideration is motivated by the frequency-dependent readout scheme considered by Kimble *et al.* [12]. Ideally, two filter cavities are able to completely cancel the radiation-pressure noise for Advanced LIGO. We investigate whether an intracavity filtering scheme with only one filter cavity can provide the same radiation-pressure noise cancellation or not. The answer turns out to be yes, but at a price of poorer sensitivity compared with frequency-dependent readout as shown in Sec. II.

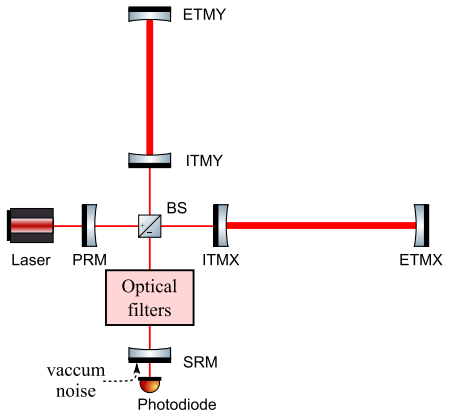

FIG. 1 (color online). The intracavity filtering scheme. Here additional optical filters are introduced between the main interferometer and the SRM. The vacuum noise enters from the dark port, and the differential motion of the ITM and end test mass (ETM) encodes the information of GWs. The power recycling mirror (PRM) is used to coherently amplify the optical power.

Motivated by the speed-meter scheme with a sloshing cavity proposed by Purdue and Chen [6], we investigate a scheme of using the intracavity filtering to create a speed meter. The scheme is similar to the sloshing speed meter but without the resonant-sideband-extraction (RSE) mirror. Interestingly, we find that the characteristic frequency ω_s for the speed response is given by the geometric mean of the arm cavity bandwidth and the sloshing-cavity bandwidth. This, as we will show in Sec. III, relieves the stringent requirement on the sloshing-cavity bandwidth in the original design proposed in [6].

Our third case is motivated by the goal of achieving a broadband enhancement in the sensitivity based on current designs of the advanced GW detectors, such as Advanced LIGO. We numerically optimize the sensitivity of the intracavity filtering scheme. With a reasonable specification for the optical loss and improvement of the classical noise, we obtain enhancement comparable to frequency-dependent squeezing, and better than the frequency-dependent readout. For the optimization, we use the cost function introduced in [13] which tries to maximize the improvement over a broad band. The details are presented in Sec. IV.

II. CASE I: CANCELING RADIATION PRESSURE NOISE

In this section, we first give a brief review of the frequency-dependent readout for evading the radiation-pressure noise presented in [12], which can be as a reference for analyzing alternative schemes, and present our first case, using the intracavity filtering scheme for canceling the radiation-pressure noise.

A. Brief review of frequency-dependent readout scheme

The input-output relation for the amplitude and phase quadratures of a general, *tuned* interferometer can be written as

$$\boldsymbol{b} = \mathbf{M}\boldsymbol{a} + \boldsymbol{D}h, \tag{1}$$

and more explicitly, by expanding out the vectors $\boldsymbol{a}$, $\boldsymbol{b}$, $\boldsymbol{D}$ and matrix $\mathbf{M}$, it is

$$\begin{bmatrix} b_1 \\ b_2 \end{bmatrix} = e^{2i\phi}\begin{bmatrix} 1 & 0 \\ -\mathcal{K} & 1 \end{bmatrix}\begin{bmatrix} a_1 \\ a_2 \end{bmatrix} + e^{i\phi}\begin{bmatrix} 0 \\ \sqrt{2\mathcal{K}} \end{bmatrix}\frac{h}{h_{\mathrm{SQL}}}. \tag{2}$$

Here $a_1(b_1)$ and $a_2(b_2)$ are the input (output) amplitude quadrature and phase quadrature, respectively, which are functions of the sideband frequency Ω with respect to the input laser frequency ω_0; ϕ is the extra phase factor; h is the GW strain and h_{SQL} the standard quantum limit (SQL) for the strain sensitivity given by [14]

$$h_{\mathrm{SQL}} = \sqrt{\frac{8\hbar}{m\Omega^2 L_{\mathrm{arm}}^2}}, \tag{3}$$

with L_{arm} being the arm length and m being the mass of test masses (TMs); $\mathcal{K}$ quantifies the measurement strength which is proportional to the optical power impinged onto the TMs and also the mechanical response of the TMs and it is given by

$$\mathcal{K} = \frac{16\omega_0\gamma I_c}{mL_{\mathrm{arm}}c\Omega^2(\Omega^2+\gamma^2)} \tag{4}$$

for a tuned, signal-recycled Michelson interferometer, with I_c the optical power inside the arm cavities and γ being the detection bandwidth jointly determined by the arm cavities and signal-recycling cavity.

The homodyne readout allows us to measure a linear combination of the output amplitude (b_1) and phase quadrature (b_2). When only the phase quadrature is measured, the readout is given by (normalized with respect to h)

$$y = \frac{e^{i\phi}h_{\mathrm{SQL}}}{\sqrt{2}}\left(-\sqrt{\mathcal{K}}a_1 + \frac{1}{\sqrt{\mathcal{K}}}a_2\right) + h \equiv \delta h + h. \tag{5}$$

Here δh is the strain-referred quantum noise with the first term being the radiation-pressure noise (also termed as backaction) and the second term being the shot noise. Its noise spectral density,[1] for uncorrelated amplitude and phase vacuum noise, can be obtained as

$$S_h = \left[\frac{\mathcal{K}}{2} + \frac{1}{2\mathcal{K}}\right]h_{\mathrm{SQL}}^2 \geq h_{\mathrm{SQL}}^2 \tag{6}$$

and is bounded by the SQL.

However, if a quadrature different from the phase quadrature is measured, the SQL is no longer the limit. Furthermore, as shown in [12], measuring the quadrature with an angle satisfying the following frequency dependence:

$$\zeta = \arctan\mathcal{K} \tag{7}$$

results in [see Eq. (2)]

$$b_\zeta = b_1\sin\zeta + b_2\cos\zeta = \left(e^{2i\phi}a_2 + e^{i\phi}\frac{\sqrt{2\mathcal{K}}h}{h_{\mathrm{SQL}}}\right)\cos\zeta. \tag{8}$$

[1]We use single-sided spectral density defined as $\langle\psi|A(\Omega)B(\Omega') + B(\Omega')A(\Omega)|\psi\rangle = \frac{1}{2}S_{AB}\delta(\Omega-\Omega')$. Here $|\psi\rangle$ is the quantum state for the optical field and the vacuum state $|0\rangle$ is used for evaluating the quantum noise which gives the cross spectral density $S_{11} = S_{22} = 1$ and $S_{12} = 0$ among the input amplitude quadrature a_1 and phase quadrature a_2.

The radiation-pressure noise is therefore canceled, leading to a sensitivity limited only by shot noise:

$$S_h^{\mathrm{BAE}} = \frac{h_{\mathrm{SQL}}^2}{2\mathcal{K}}. \tag{9}$$

To achieve above frequency dependence, one can employ a cascade of filter cavities which rotates the quadrature depending on the frequency, as shown in [12]. Specifically, the effects of filter cavities on the quadratures can be described by the following matrix:

$$\mathbf{M}_f = e^{i\phi_f}\begin{bmatrix} \cos\zeta_f & -\sin\zeta_f \\ \sin\zeta_f & \cos\zeta_f \end{bmatrix}, \tag{10}$$

with the rotation angle ζ_f and the phase shift ϕ_f being

$$\zeta_f = \frac{\alpha_+ + \alpha_-}{2}, \qquad \phi_f = \frac{\alpha_+ - \alpha_-}{2}, \tag{11}$$

where α_+ and α_- are phase shifts of upper and lower sidebands induced by the filter cavity. In particular, in the narrow band approximation ($\Omega \ll \omega_{\mathrm{fsr}}$ with ω_{fsr} being the free spectral range), for one filter cavity we have

$$e^{i\alpha_\pm(\Omega)} = -\frac{\Omega \mp \Delta_f \mp i\gamma_f}{\Omega \mp \Delta_f \pm i\gamma_f}, \tag{12}$$

with Δ_f and γ_f being the cavity detuning and bandwidth, respectively.

A proper choice of the filter cavity parameters enables the desired frequency-dependent rotation of the quadratures. As proven in Appendix A of [6] [see Eq. (A12) in their paper], when the required $\tan\zeta$ of the rotation angle is a rational function in Ω^2 with the highest order of Ω^{2n}, n filter cavities are needed. For obtaining $\tan\zeta = \mathcal{K}$ in Eq. (4), which is a rational function of Ω^2 with the highest order being Ω^4, two filter cavities are therefore required.

B. Intracavity filtering for canceling radiation-pressure noise

In Fig. 2 we show the corresponding intracavity filtering scheme in which one filter cavity and a RSE mirror are placed inside the signal-recycling cavity. The RSE mirror is used to effectively remove the frequency response of the arm cavities such that only one filter cavity is needed for canceling the radiation-pressure noise (the highest frequency dependence of $\mathcal{K}$ becomes Ω^2 instead of Ω^4). More explicitly, the filter cavity sees an input-output relation for the optical field in a form similar to Eq. (2), but with $\mathcal{K}$ being replaced by

$$\kappa = \frac{8I_c\omega_0}{mc^2\Omega^2} \equiv \frac{\Omega_q^2}{\Omega^2}, \tag{13}$$

where Ω_q is a characteristic frequency at which the sensitivity curve touches the SQL.

To obtain the condition for canceling radiation-pressure noise, we first look at the combined effect of $\mathbf{M}$ [see Eq. (2), replacing $\mathcal{K}$ by κ] and $\mathbf{M}_f$ inside the signal-recycling cavity. It is described by $\mathbf{M}_{\mathrm{tot}} \equiv \mathbf{M}_f\mathbf{M}\mathbf{M}_f$ which reads

$$\mathbf{M}_{\mathrm{tot}} = e^{2i\phi_{\mathrm{tot}}}\begin{bmatrix} \cos 2\zeta_f + \frac{\kappa}{2}\sin 2\zeta & -\sin 2\zeta - \kappa\sin^2\zeta \\ \sin 2\zeta_f - \kappa\cos^2\zeta_f & \cos 2\zeta_f + \frac{\kappa}{2}\sin 2\zeta_f \end{bmatrix}, \tag{14}$$

with $\phi_{\mathrm{tot}} = \Omega L_{\mathrm{arm}}/c + \phi_f$. In order to remove the radiation-pressure noise from the phase quadrature as the usual frequency-dependent readout, we require the above matrix to be upper triangular, i.e.,

$$-\kappa\cos^2\zeta_f + \sin 2\zeta_f = 0 \tag{15}$$

or equivalently,

$$\tan\zeta_f = \kappa/2, \tag{16}$$

which is achieved by choosing the filter cavity detuning and bandwidth to be

$$\Delta_f = \gamma_f = \Omega_q/2. \tag{17}$$

Under this condition, the above matrix simply becomes

$$\mathbf{M}_{\mathrm{tot}} = e^{2i\phi_{\mathrm{tot}}}\begin{bmatrix} 1 & -\kappa \\ 0 & 1 \end{bmatrix}. \tag{18}$$

Since there is no additional rotation to $\mathbf{M}_{\mathrm{tot}}$ during the propagation (see the block diagram in Fig. 2), if we measure the output phase quadrature b_2, which only depends on the input phase quadrature a_2, we shall obtain a sensitivity only limited by the shot noise. The final input-output relation is given by

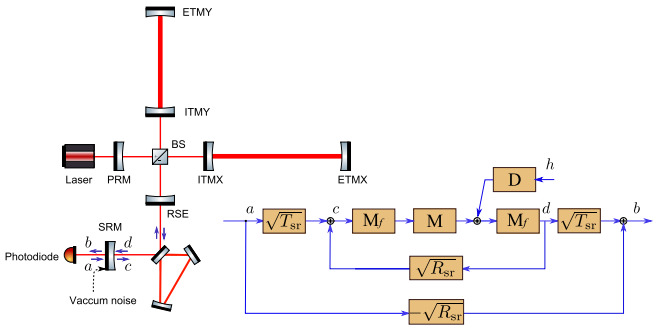

FIG. 2 (color online). An intracavity filtering scheme with a single filter together with a RSE mirror for canceling the radiation-pressure noise (left) and its block diagram (right). Blocks M, M_f and $\mathbf{D}$ are defined in Eqs. (1) and (10). T_{sr} and R_{sr} are the transmissivity and reflectivity of the SRM.

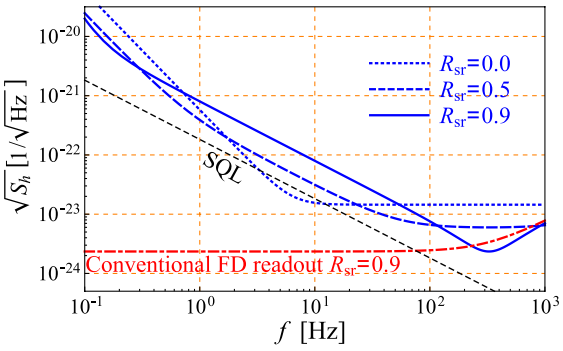

FIG. 3 (color online). The sensitivity of the intracavity filtering scheme for evading radiation-pressure noise with different signal-recycling mirror reflectivities (blue) in comparison with the conventional frequency-dependent readout (FD) scheme proposed in [12] which uses two additional filter cavities to filter the output from the signal-recycling mirror.

$$\boldsymbol{b} = [-\sqrt{R_{\rm sr}}\mathbf{I} + T_{\rm sr}\mathbf{M}_c\mathbf{M}_{\rm tot}]\boldsymbol{a} + \sqrt{T_{\rm sr}}\mathbf{M}_c\mathbf{M}_f\mathbf{D}h, \quad (19)$$

with $\mathbf{M}_c \equiv [\mathbf{I} - \sqrt{R_{\rm sr}}\mathbf{M}_{\rm tot}]^{-1}$ and $\mathbf{I}$ the identity matrix.

Naively one might expect that by just placing *one* filter cavity inside the signal-recycling cavity we can achieve the same sensitivity as the frequency-dependent readout. However, as shown in Fig. 3, this is not the case, and the performance is poorer. Moreover, the sensitivity at intermediate frequencies decreases as we increase the reflectivity of the signal-recycling mirror; even when the reflectivity goes to zero (no signal-recycling mirror), we do not recover the frequency-dependent readout.

To understand the sensitivity degradation in comparison with the conventional frequency-dependent readout, we first look at the case of $R_{\rm sr} = 0$. We can write down the input-output relation for the phase quadrature explicitly as (normalized with respect to strain)

$$y_2 = \frac{e^{i\phi_{\rm tot}}h_{\rm SQL}}{\sqrt{2\kappa}\cos\zeta_f}a_2 + h \equiv \delta h + h. \quad (20)$$

At low frequencies $\Omega \ll \Omega_q$, $\kappa \gg 1$, $\cos\zeta_f \sim 1/\kappa$ and the strain-referred noise term δh reads

$$\delta h|_{\Omega\ll\Omega_q} \approx \sqrt{\frac{\kappa}{2}}h_{\rm SQL}a_2 \propto \frac{h_{\rm SQL}}{\Omega}a_2. \quad (21)$$

Therefore, even though it is a shot-noise limited sensitivity, the spectrum of the shot noise is not flat and increases at low frequencies as shown by the dotted line in Fig. 3. This comes from the additional rotation of the input vacuum field by the filter cavity, which is absent in the usual frequency-dependent readout [see Eq. (8)].

For $R_{\rm sr} \neq 0$, the expression for the output phase quadrature (strain-referred) is

$$y_2 = \frac{e^{i\phi_{\rm tot}}(1 - \sqrt{R_{\rm sr}}e^{2i\phi_{\rm tot}})h_{\rm SQL}}{\sqrt{2T_{\rm sr}\kappa}\cos\zeta_f}a_2 + h \equiv \delta h + h, \quad (22)$$

with the phase factor being

$$e^{2i\phi_{\rm tot}} = e^{2i\Omega L_{\rm arm}/c}\frac{(\Omega - i\Omega_q/2)^2 - \Omega_q^2/4}{(\Omega + i\Omega_q/2)^2 - \Omega_q^2/4}. \quad (23)$$

To understand the behavior as shown in Fig. 3, we consider the case of $T_{\rm sr} \ll 1$ at three different frequency regimes: (i) *at very low frequencies* $\Omega \ll \Omega_q/2$, we have $e^{2i\phi_{\rm tot}} \sim 1$ and $\cos\zeta \sim 1/\kappa$. We can therefore obtain

$$\delta h|_{\Omega\ll\Omega_q/2} \approx \sqrt{\frac{T_{\rm sr}\kappa}{8}}h_{\rm SQL}a_2 \propto \sqrt{T_{\rm sr}}\frac{h_{\rm SQL}}{\Omega}a_2. \quad (24)$$

The frequency dependence is the same as $R_{\rm sr} = 0$ [see Eq. (21)] but with an additional factor $\sqrt{T_{\rm sr}}$—the smaller $T_{\rm sr}$ the better the sensitivity; (ii) *at intermediate frequencies* around $\Omega_q/2$, we have

$$1 - \sqrt{R_{\rm sr}}e^{2i\phi_{\rm tot}} \approx \frac{2i\Omega\Omega_q}{(\Omega + i\Omega_q/2)^2 - \Omega_q^2/4}. \quad (25)$$

At frequencies smaller than (yet still around) $\Omega_q/2$, it is approximated to be $-4i\Omega/\Omega_q$; at higher frequencies $\Omega \gtrsim \Omega_q/2$, it approximately equals to $2i\Omega_q/\Omega$. Therefore, we obtain the strain-referred noise term:

$$\delta h|_{\Omega\lesssim\Omega_q/2} \propto \frac{\Omega\sqrt{\kappa}}{\sqrt{T_{\rm sr}}}h_{\rm SQL}a_2 \propto \frac{h_{\rm SQL}}{\sqrt{T_{\rm sr}}}a_2, \quad (26)$$

and

$$\delta h|_{\Omega\gtrsim\Omega_q/2} \propto \frac{1}{\Omega\sqrt{\kappa}\sqrt{T_{\rm sr}}}h_{\rm SQL}a_2 \propto \frac{h_{\rm SQL}}{\sqrt{T_{\rm sr}}}a_2, \quad (27)$$

where we used the fact that $\Omega\sqrt{\kappa} \propto \Omega^0$. This explains why the spectrum is parallel to the SQL around intermediate frequencies. We also notice that the sensitivity decreases as we increase the reflectivity (smaller $T_{\rm sr}$); (iii) *at very high frequencies* $\Omega \gg \Omega_q/2$, we have

$$1 - \sqrt{R_{\rm sr}}e^{2i\phi_{\rm tot}} \approx T_{\rm sr}/2 - 2i\Omega L_{\rm arm}/c, \quad (28)$$

and

$$\delta h|_{\Omega\gg\Omega_q/2} \propto \frac{T_{\rm sr} - 4i\Omega L_{\rm arm}/c}{\sqrt{T_{\rm sr}\kappa}}h_{\rm SQL}a_2. \quad (29)$$

At very high frequencies, the noise spectrum increases as frequency Ω, which matches the spectrum behavior as shown in Fig. 3 (the blue solid curve).

It is worthy mentioning that if the filter cavity is tuned to be resonant, instead of detuned for evading the

radiation-pressure noise, the above scheme becomes a speed meter, even when the RSE mirror is removed, as we will discuss in Sec. III.

III. CASE II: REALIZING A SPEED METER

In this section, we investigate the intracavity filtering scheme as a speed meter, inspired by the speed-meter scheme proposed by Purdue and Chen [6], which introduced an additional sloshing cavity to create speed response.

A. Brief review of the speed meter with sloshing cavity

The corresponding speed-meter scheme is shown in Fig. 4, where a sloshing cavity combined with a RSE mirror is added to the interferometer output. Again the RSE mirror is applied to cancel the effect of the ITMs of the arm cavities, and it has the same transmissivity as the ITMs. In this case the speed response then can be understood qualitatively by using the model of two coupled cavity modes as shown in the right part of Fig. 4. In particular, the cavity mode c_a corresponds to the optical field inside the arm cavities, and the cavity mode c_b is the field inside the sloshing cavity. These two are coupled via the sloshing mirror with a characteristic coupling rate given by the sloshing frequency ω_s, which is defined as

$$\omega_s = \frac{c\sqrt{T_s}}{2\sqrt{L_{\rm arm}L_s}}, \tag{30}$$

with L_s being the length of the sloshing cavity and T_s being the transmissivity of the sloshing mirror.

The classical equations of motion for these two cavity modes can be written as

$$\dot{c}_a + \gamma c_a = -iGx - i\omega_s c_b, \tag{31}$$

$$\dot{c}_b = -i\omega_s c_a. \tag{32}$$

Here $\gamma = 4cT_0/L_{\rm arm}$ is the signal extraction rate and G quantifies the response of the cavity mode to the test mass displacement. Solving these two equations in the frequency domain yields

$$c_a(\Omega) = \frac{G\Omega}{\Omega^2 - \omega_s^2 + i\Omega\gamma}x(\Omega). \tag{33}$$

At low frequencies $\Omega \ll \omega_s$ and a small extraction rate $\gamma < \omega_s$, we obtain

$$c_a(\Omega) \approx -\frac{G\Omega}{\omega_s^2}x(\Omega) \propto -i\Omega x(\Omega), \tag{34}$$

which implies a speed response.

The exact input-output relation for such a scheme is given in [6] [see Eqs. (12), (13) and (14) in the paper], and have a similar form as Eq. (2) with $\mathcal{K}$ given by

$$\mathcal{K}_{\rm sm} = \frac{16\omega_0 I_c}{mL_{\rm arm}c|\Omega^2 - \omega_s^2 + i\gamma\Omega|^2}. \tag{35}$$

Notice that $\mathcal{K}_{\rm sm}$ is nearly a constant at low frequencies instead of having a strong frequency dependence. This means that in order to evade the radiation-pressure noise at low frequencies by satisfying Eq. (7), one can simply measure a quadrature that is frequency independent

$$\zeta_{\rm sm} = \arctan \mathcal{K}_{\rm sm}|_{\Omega\to 0}. \tag{36}$$

A frequency-dependent readout is only needed when a better sensitivity is required particularly at high frequencies. This is due to the fact that high-frequency sensitivity is normally degraded if $\zeta_{\rm sm}$ is different from zero (which represents the phase quadrature).

B. Intracavity filtering as a speed meter

Figure 5 shows two equivalent intracavity filtering speed-meter schemes without the RSE mirror. In terms of complexity, it is the same as the previous sloshing-cavity scheme, but the sensitivity performance is different. As we will show, it has two interesting features. The *first* one is

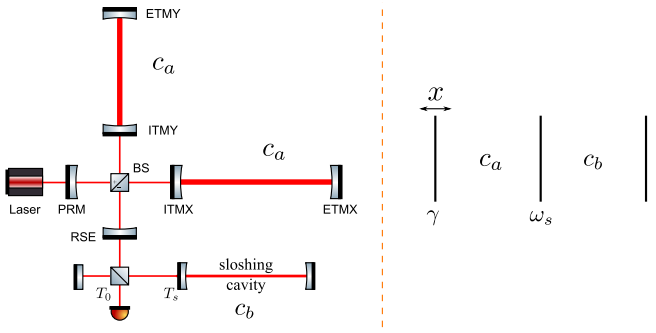

FIG. 4 (color online). The speed meter realized by adding an additional sloshing cavity at the output port proposed in [6] (left) and its simplified two-cavity-mode model (right).

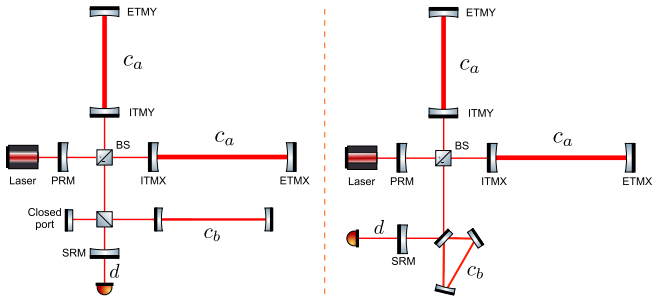

FIG. 5 (color online). Two equivalent intracavity filtering schemes as speed meter. Compared with the speed meter with a sloshing cavity shown in Fig. 4, there is no RSE mirror but a signal-recycling mirror SRM.

that it also has a speed response and the characteristic frequency ω_s, up to which the speed response dominates, is given by

$$\omega_s = \frac{c\sqrt{T_{\rm ITM}T_s}}{2\sqrt{L_{\rm arm}L_s}} = \sqrt{\gamma_{\rm arm}\gamma_s}. \tag{37}$$

This differs from Eq. (30) by an extra factor of $\sqrt{T_{\rm ITM}}$, the transmissivity coefficient of the arm cavity ITMs. Thus the sloshing frequency is determined by the compound mirror formed by the ITMs and the sloshing mirror. This feature makes it appealing in the sense that we can realize a speed meter with a relatively short sloshing cavity. For example, given the ITM transmittance $T_{\rm ITM} = 0.01$ and $T_s = 900$ ppm, we can set the sloshing frequency around 100 Hz for a 100 m sloshing cavity. However, this is very challenging for the speed meter proposed in [6], in which case the sloshing mirror transmittance T_s needs to be 90 ppm given a 100 m sloshing cavity. The *second* interesting feature is that it can also have a position response at low frequencies when the parameters are chosen properly. This can possibly provide a way to create a *local oscillator* for a practical readout scheme similar to the direct current (DC) readout realization described in [15].

To perform a detailed analysis of the scheme's quantum noise, one can use the standard input-output formalism by writing down the propagation equations for the fields and solve a set of linear equations in the frequency domain. Instead, here we will follow the approach given in [16] by mapping parameters of the optics into several characteristic quantities, and using the narrow band approximation to define some effective modes. The advantage of this method is that it allows us to gain a clearer insight into the dynamics of the intracavity filtering scheme. We define (i) c_a—the differential mode of the two arm cavities; (ii) c_b—the cavity mode inside the sloshing cavity; (iii) d—the external field; and (iv) ω_s, γ_a and γ_b—the characteristic frequencies for the coupling between c_a, c_b and d, as illustrated schematically in Fig. 5. These characteristic frequencies, ω_s, ω_a, ω_b, γ_a and γ_b, are related to the parameters of the optical components, which are shown explicitly in the Appendix.

We can then write down the Hamiltonian for the intracavity filtering scheme consisting of two optical modes and one test mass with reduced mass m, which reads

$$\hat{\mathcal{H}} = \hat{\mathcal{H}}_0 + \hat{\mathcal{H}}_{\rm int} + \hat{\mathcal{H}}_{\rm ext} + \hat{\mathcal{H}}_{\rm GW}. \tag{38}$$

It contains four parts:

(i) The free Hamiltonian $\hat{\mathcal{H}}_0$ reads

$$\hat{\mathcal{H}}_0 = \hbar\omega_a\hat{c}_a^\dagger\hat{c}_a + \hbar\omega_b\hat{c}_b^\dagger\hat{c}_b + \frac{\hat{p}^2}{2m}. \tag{39}$$

(ii) The interaction Hamiltonian $\hat{\mathcal{H}}_{\rm int}$ is

$$\hat{\mathcal{H}}_{\rm int} = \hbar G_a\hat{x}\hat{c}_a + \hbar\omega_s\hat{c}_a^\dagger\hat{c}_b + \text{H.c.}, \tag{40}$$

where "H.c." denotes the *Hermitian conjugate*. The first term represents the interaction between the cavity mode $\hat{c}_a$ and the test mass $\hat{x}$ via radiation pressure with $G_a = \omega_0\bar{c}_a/L_{\rm arm}$ and $\bar{c}_a$ being the steady-state amplitude of $\hat{c}_a$ due to the coherent pumping of the laser. The second term describes the coupling between the two cavity modes with the coupling rate given by ω_s.

(iii) The interaction Hamiltonian $\hat{\mathcal{H}}_{\rm ext}$ between the cavity modes and the external field $\hat{d}$ reads

$$\hat{\mathcal{H}}_{\rm ext} = i\hbar(\sqrt{2\gamma_a}\hat{a}^\dagger + \sqrt{2\gamma_b}\hat{b}^\dagger)\hat{d}e^{-i\omega_0 t} + \text{H.c.} \tag{41}$$

(iv) The energy $\hat{\mathcal{H}}_{\rm GW}$ from the interaction between the test mass and the GW tidal force $F_{\rm GW}$ is given by

$$\hat{\mathcal{H}}_{\rm GW} = -\hat{x}F_{\rm GW}. \tag{42}$$

Given the above Hamiltonian, we can obtain the corresponding equations of motion. Specifically, for the test mass, we obtain

$$m\ddot{\hat{x}} = \hat{F}_{\rm rad} + F_{\rm GW}, \tag{43}$$

with the radiation-pressure force $\hat{F}_{\rm rad}$ defined as

$$\hat{F}_{\rm rad} \equiv -\hbar G_a(\hat{c}_a + \hat{c}_a^\dagger). \tag{44}$$

For the cavity modes $\hat{c}_a$ and $\hat{c}_b$, we have

$$\dot{\hat{c}}_a + (\gamma_a + i\Delta_a)\hat{c}_a = -iG_a\hat{x} - i\omega_s\hat{c}_b + \sqrt{2\gamma_a}\hat{d}_{\rm in}, \tag{45}$$

$$\dot{\hat{c}}_b + (\gamma_b + i\Delta_b)\hat{c}_b = -i\omega_s\hat{c}_a + \sqrt{2\gamma_b}\hat{d}_{\rm in}. \tag{46}$$

The above detuning frequency $\Delta_{a,b}$ is defined as $\Delta_j \equiv \omega_j - \omega_0 (j = a, b)$. The interferometer output is related to the cavity modes through the standard input-output relation:

$$\hat{d}_{\rm out} = -\hat{d}_{\rm in} + \sqrt{2\gamma_a}\hat{c}_a + \sqrt{2\gamma_b}\hat{c}_b. \tag{47}$$

These equations can be solved in the frequency domain, and are generally quite lengthy but straightforward. Here we focus on the tuned case of $\Delta_a = \Delta_b = 0$, which gives

$$\hat{c}_a = \frac{G_a(\Omega + i\gamma_b)\hat{x} + [\sqrt{2\gamma_a}(\gamma_b - i\Omega) - i\sqrt{2\gamma_b}\omega_s]\hat{d}_{\rm in}}{(\Omega + i\gamma_a)(\Omega + i\gamma_b) - \omega_s^2}, \tag{48}$$

$$\hat{c}_b = \frac{G_a\omega_s\hat{x} + [\sqrt{2\gamma_b}(\gamma_a - i\Omega) - i\sqrt{2\gamma_a}\omega_s]\hat{d}_{\rm in}}{(\Omega + i\gamma_a)(\Omega + i\gamma_b) - \omega_s^2}, \quad (49)$$

and the radiation-pressure noise reads

$$\hat{F}_{\rm rad} = \frac{2\hbar G_a[\sqrt{\gamma_a}(\gamma_b - i\Omega)\hat{d}_1 + \sqrt{\gamma_b}\omega_s\hat{d}_2]}{(\Omega + i\gamma_a)(\Omega + i\gamma_b) - \omega_s^2}, \quad (50)$$

with $\hat{d}_1 \equiv (\hat{d}_{\rm in} + \hat{d}_{\rm in}^\dagger)/\sqrt{2}$ and $\hat{d}_2 \equiv (\hat{d}_{\rm in} - \hat{d}_{\rm in}^\dagger)/\sqrt{2}i$.

The response to the test-mass displacement at the output reads

$$\hat{d}_{\rm out}^{|x}(\Omega) = \frac{G_a[\sqrt{2\gamma_a}\Omega + \sqrt{2\gamma_b}(i\sqrt{\gamma_a\gamma_b} + \omega_s)]\hat{x}(\Omega)}{(\Omega + i\gamma_a)(\Omega + i\gamma_b) - \omega_s^2}. \quad (51)$$

As we can see, the first term in the bracket of the numerator is proportional to Ω, which gives the speed response, while the remaining term proportional to $\sqrt{\gamma_b}$ gives the linear displacement response. Therefore, it contains a mix of speed and displacement response. This is similar to the polarizing Sagnac interferometer with imperfect polarizing beam splitter [15], and it implies a potential local oscillator for a homodyne detection can be extracted. The turning frequency $\Omega_{\rm turn}$, at which the speed response becomes dominant, is given by [see Eq. (51)]:

$$\Omega_{\rm turn} = \omega_s\sqrt{\frac{\gamma_b}{\gamma_a}}. \quad (52)$$

In the limit of $\gamma_b \to 0$, it approaches the speed meter

$$\hat{d}_{\rm out}^{|x}(\Omega)|_{\gamma_b\to 0} = \frac{\sqrt{2\gamma_a}G_a\Omega}{\Omega^2 + i\gamma_a\Omega - \omega_s^2}\hat{x}(\Omega), \quad (53)$$

with a sloshing frequency given by Eq. (37) [with proper phase chosen (see its definition in Eq. (A9)].

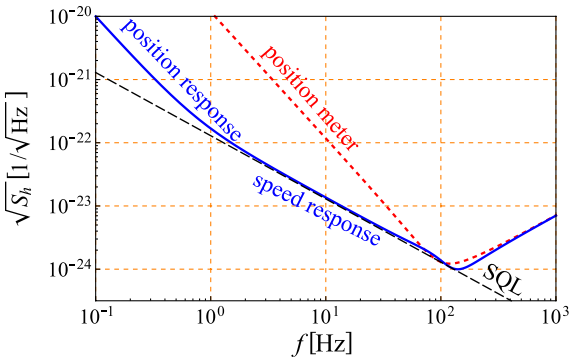

FIG. 6 (color online). The sensitivity curve for the intracavity filtering scheme (blue solid) in comparison with the conventional position meter (red dotted). There is a smooth transition from the position response to the speed response.

TABLE I. A table showing the power transmissivity (and the reflection phase) of relevant mirrors in the three-port junction as shown in Fig. 10 (the Appendix), resulting in the sensitivity (blue) in Fig. 6. The left column values refer to a model combining the SRM, the sloshing mirror, and the arm cavity ITMs. The right-hand column values correspond to a design without the SRM, however, giving the same sensitivity.

Mirror†	With SRM	Without SRM
Sloshing mirror	0.0048(0.0)	0.00080(0.0)
ITM	$0.012(\pi)$‡	$0.068(\pi)$
SRM	0.50(0.0)	1.0(0.0)

†Here we only specify the parameters for the left scheme in Fig. 5.

‡The phase of the ETMs needs to be π correspondingly to ensure the resonance of the arm cavities.

In Fig. 6, we show the resulting sensitivity by choosing $\gamma_a/2\pi = \omega_s/2\pi = 100$ Hz and $\gamma_a/2\pi = 0.007$ Hz (blue). Indeed, at low frequencies the sensitivity curve is similar to that of a position meter (red) and it smoothly transits to the speed-meter sensitivity in the intermediate frequencies. Given those parameters, the turning frequency $\Omega_{\rm turn}$ is around 1 Hz which matches the blue curve.

These characteristic frequencies can be mapped to parameters for the optics by using their definitions in Eqs. (A9) and (A10) (the Appendix). We summarize these parameters in Table I. Two possible designs are presented in terms of including the SRM or not. From the mirror parameters shown in Table I, we conclude that an intracavity filtering scheme could be implemented as an alternative speed meter without stringent design requirements. Meanwhile, a scheme in the absence of the SRM could also have a speed-meter response, however, requiring a high reflection sloshing mirror.

IV. CASE III: ACHIEVING BROADBAND SENSITIVITY

In the previous two sections, we have been focusing our investigation on two specific intracavity filtering schemes; both offer explicit analytical expressions that help to gain clear insights. However, these particular models cover only a small parameter space of all possible intracavity filtering schemes. In this section we present a numerical optimization with the aim to maximize a certain cost function as to evaluate the overall limits to the performance of this scheme.

For optimization, we use the cost function introduced in [13] including realistic nonquantum noises (e.g., suspension and mirror coating thermal noise):

$$\mathcal{C}(\boldsymbol{x}) = \left\{\int_{f_{\rm min}}^{f_{\rm max}} {\rm d}(\log_{10} f)\log_{10}\left[\frac{h_{\rm ref}}{h_{\rm intra}(\boldsymbol{x})}\right]\right\}^{-1}, \quad (54)$$

where $[f_{\rm min}, f_{\rm max}]$ is the frequency range of the optimization; $\boldsymbol{x}$ is the set of optical parameters that can be tuned by the algorithm, in particular the parameters of the compound

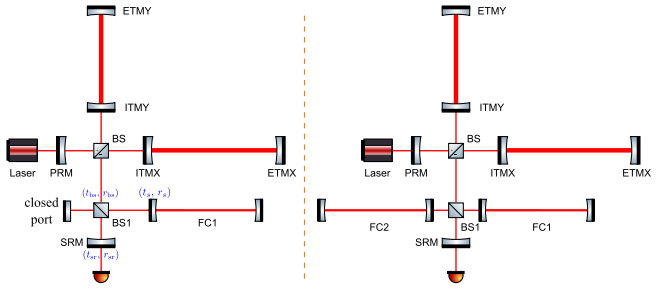

FIG. 7 (color online). The intracavity filtering schemes with one filter cavity and a closed port (left) and two filter cavities (right), for numerical optimization using the cost function equation (54).

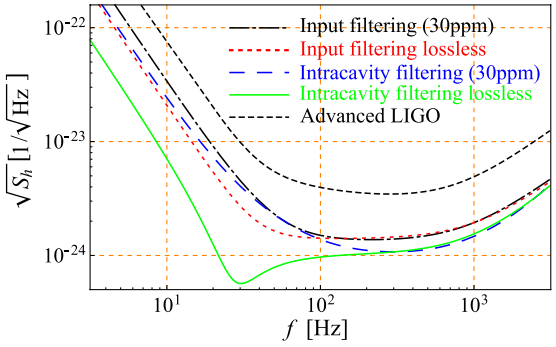

FIG. 8 (color online). Plot comparing the numerically optimized quantum-noise spectral density of an intracavity filtering scheme [see Fig. 7 (left) or Fig. 5] with an input-filtering scheme [12], which uses frequency-dependent squeezing to reduce quantum noise over a broad frequency band. The quantum-noise spectral density of Advanced LIGO is chosen as our reference [1].

optics, including transmissivity and reflectivity of the filter cavity, the SRM, and the BS1; h_{ref} is the square root of the total noise spectral density—the sum of quantum-noise and classical-noise spectral densities—of a reference design

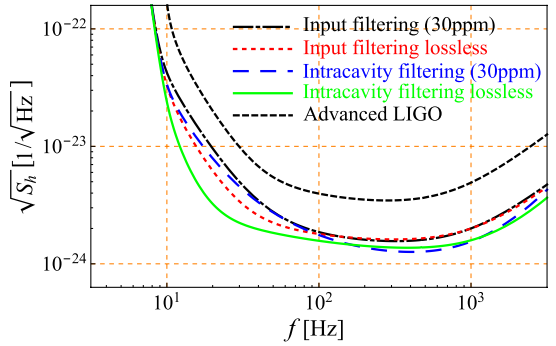

FIG. 9 (color online). Plot showing the numerically optimized total noise spectrum of an intracavity filtering scheme compared to an input-filtering case. Here classical noises such as thermal noise, gravity gradient noise and seismic noise are included based on the Advanced LIGO baseline design [1,17].

TABLE II. A table summarizing the optimal power transmissivity (and the reflection phase) of the optics in the intracavity filtering scheme shown in Fig. 7 (left). The lossless values refer to an idealized model. The 30 ppm column provides parameters based on a optical loss at the mirrors of 30 ppm. The reflectivity coefficients are complex numbers indicating the phase shift of the propagation as shown in Fig. 10.

Parameter	Lossless case	Lossy case
FC input mirror	0.0057(0.0)	0.0090(0.0)
SRM	0.040(−0.045)	0.027(−0.018)
BS1	0.25(−0.017)	0.13(−0.0032)

(which can be the Advanced LIGO baseline design); and h_{intra} is the square root of the total noise spectral density of the intracavity filtering scheme. We will maximize the results by integrating over $\log f$ instead of f to give higher weight to low-frequency sensitivity.

We initially considered an intracavity filtering scheme with two optical cavities placed inside the signal-recycling cavity as shown in the right-hand side of Fig. 7. However, the optimization results suggested that a configuration as shown in the left-hand side of Fig. 7 with only one filter cavity is sufficient to achieve an equivalently good result. The outcomes of the optimization are provided in Fig. 8 and Fig. 9, where the dashed black curve shows the noise spectral density of Advanced LIGO as a reference [1,17]. The optimized parameters are summarized in Table II. The intracavity filtering scheme with one optical cavity is able to reduce quantum noise over a broadband as shown in Fig. 8. For an ideal case, it is much better than an input-filtering scheme shown as the green solid curve against the red solid curve. In addition, we compare the quantum noise of the ideal lossless case (green) with a model including 30 ppm mirror loss (blue). We found that optical losses degrade low-frequency quantum noise in the intracavity filtering scheme and its susceptibility to loss is similar to the input-filtering scheme which is shown as the black solid curve in the figure (for both schemes, the filter cavity length is assumed to be 100 m). Considering a 30 ppm mirror loss, the performance of an intracavity filtering scheme is slightly better than an input-filtering scheme. Figure 9 compares the sensitivity of the input-filtering and intracavity filtering schemes respectively given that Advanced LIGO baseline design is applied with other classical noises, e.g., thermal noise, gravity gradient noise and seismic noise [1] being included.

V. CONCLUSIONS

Previous work has shown that the quantum noise of advanced gravitational-wave detectors can be reduced over a broad frequency band by modifying the input optics (input filtering) or output optics (output filtering) [12]. We have investigated an alternative filtering scheme—intracavity

filtering, placing an optical cavity inside the signal-recycling cavity, as a practical implementation for future GW detectors.

We first considered the intracavity filtering as an alternative method to cancel the radiation-pressure noise, hoping to reproduce the excellent low-frequency quantum-noise performance realized by the ideal frequency-dependent readout. However, it turned out that the filter cavity produces a frequency-dependent phase shift that significantly reduced the sensitivity at intermediate frequencies. More explicitly, we have shown the resulting noise spectrum: (i) at low frequencies, is scaled as $\sqrt{T_{\rm sr}}/\Omega^2$, (ii) at intermediate frequencies as $1/(\Omega\sqrt{T_{\rm sr}})$, and (iii) at high frequencies as $\Omega/\sqrt{T_{\rm sr}}$.

We continued our investigation and considered the intracavity filtering as a speed meter similar to the one proposed in [6,18]. Such a scheme, first of all, does not require a RSE mirror. More important, it eases the stringent requirement of the sloshing-cavity design presented in [6], as the characteristic frequency for the speed response is not determined by the sloshing mirror only, but is now also related to the transmissivity of the arm cavity ITM ($T_{\rm ITM}$). In particular, the requirement on low transmissivity of the sloshing mirror can be relieved by a factor of $\sqrt{T_{\rm ITM}}$. We also found that the quantum noise of this scheme, at low frequencies, shows a position-meter-like response and then smoothly transits to a speed-meter response in the intermediate frequencies.

The quantum-noise behavior of the intracavity filtering varies when choosing different optical filters inside the signal-recycling cavity. We numerically optimize the intracavity filtering scheme, aiming at reducing quantum noise over a broad frequency band. This optimization uses the Advanced LIGO sensitivity as a reference and assumed reduced classical noises (such as seismic noise, suspension and mirror thermal noise). We showed that, with reasonable optical losses, for instance 30 ppm per mirror, the quantum noise of an intracavity filtering scheme is comparable to the frequency-dependent squeezing, so that this scheme can be considered as an potential alternative.

In summary, even though an intracavity filter scheme is not able to completely evade the radiation-pressure noise, we found its implementation as a speed meter eases the tight requirements of the cavity design compared to a sloshing-cavity speed meter. Meanwhile, its mixed position and speed response encourages future investigation of an intracavity filter scheme as a practical alternative for GW detectors. Additionally, the global optimization of an intracavity filtering produced a similarly low quantum-noise behavior as frequency-dependent squeezing.

ACKNOWLEDGEMENTS

We would like to thank Farid Khalili, Stefan Danilishin, Sergey Vyatchanin and members in the LIGO-MQM discussion group for discussions. We also thank Rana Adhikari, Matthew Evans, Stefan Ballmer and members in the AIC working group for fruitful discussions. We thank Frank Brückner for comments. M. W. and A. F. have been supported by the Science and Technology Facilities Council (STFC). H. M. and Y. C. are supported by the National Science Foundation (NSF) Grants No. PHY-0555406, No. PHY-0956189, No. PHY-1068881, as well as the David and Barbara Groce startup fund at Caltech, and the Institute for Quantum Information and Matter, a Physics Frontier Center with funding from the NSF and the Gordon and Betty Moore Foundation.

APPENDIX: INPUT-OUTPUT RELATION FOR THE THREE-PORT JUNCTION IN THE INTRACAVITY FILTERING SCHEME

In this section we provide details for the input-output relation in the intracavity filtering scheme and define the characteristic frequencies used in the Hamiltonian in Sec. III.

In Fig. 10, we show the reflectivity for each optics and its convention of sign. By using the junction condition on each optics, we obtain

$$\boldsymbol{v}^{\rm ref} = \mathbf{M}_t \boldsymbol{v}^{\rm in}, \tag{A1}$$

with $\boldsymbol{v}^{\rm ref} = [c_a^{\rm ref}, c_b^{\rm ref}, d^{\rm ref}]^{\rm T}$ and $\boldsymbol{v}^{\rm in} = [c_a^{\rm in}, c_b^{\rm in}, d^{\rm in}]^{\rm T}$ (the superscript T denotes the transpose) and $\mathbf{M}_t$ being the transfer matrix. The transfer matrix has the following property:

$$\mathbf{M}_t = \mathbf{M}_t^{\rm T}, \qquad \mathbf{M}_t \mathbf{M}_t^{\dagger} = \mathbf{I}, \tag{A2}$$

which means that $\mathbf{M}_t$ is a *symmetric unitary* matrix. This gives the Stokes relation for such a three-port linear optics. More specifically, the elements of $\mathbf{M}_t$ in terms of the reflectivity and transmissivity of each optics are given by

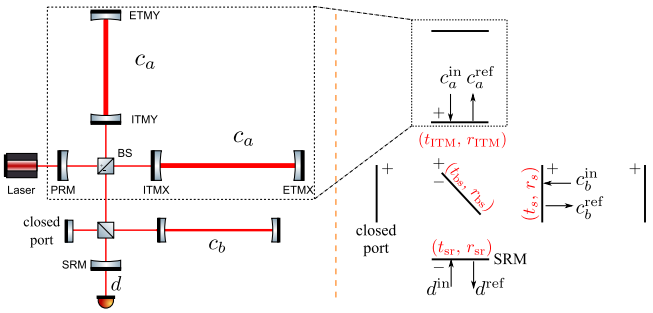

FIG. 10 (color online). Diagram illustrating the three-port junction that we are interested in. We map the two arm cavities into a single cavity (denoted by the dashed box), following [16]. Here r_i (complex) and t_i (real) are the amplitude reflectivity and transmissivity of the optics. The sign of convention for the reflectivity are indicated by $\pm$—the amplitude reflectivity on the positive side is r and the minus side is $-r^*$ (complex conjugate).

$$\mathbf{M}_{11} = \mathcal{D}^{-1}[r_{\mathrm{ITM}} - r_s^* r_{\mathrm{bs}}^2 - r_{\mathrm{ITM}} r_{\mathrm{sr}} r_{\mathrm{bs}}^{*2} + (r_{\mathrm{sr}} + r_{\mathrm{ITM}} r_s^*) t_{\mathrm{bs}}^2 + r_s^* r_{\mathrm{sr}}], \tag{A3}$$

$$\mathbf{M}_{12} = \mathcal{D}^{-1}(r_{\mathrm{bs}} - r_{\mathrm{sr}} r_{\mathrm{bs}}^*) t_{\mathrm{ITM}} t_s, \tag{A4}$$

$$\mathbf{M}_{13} = \mathcal{D}^{-1}(1 + r_s^*) t_{\mathrm{ITM}} t_{\mathrm{sr}} t_{\mathrm{bs}}, \tag{A5}$$

$$\mathbf{M}_{22} = \mathcal{D}^{-1}[r_s - r_{\mathrm{ITM}}^* r_{\mathrm{bs}}^2 - r_s r_{\mathrm{sr}} r_{\mathrm{bs}}^{*2} + (1 + r_{\mathrm{ITM}}^* r_s r_{\mathrm{sr}}) t_{\mathrm{bs}}^2 + r_{\mathrm{ITM}}^* r_{\mathrm{sr}}], \tag{A6}$$

$$\mathbf{M}_{23} = \mathcal{D}^{-1}(-r_{\mathrm{bs}}^* - r_{\mathrm{ITM}}^* r_{\mathrm{bs}}) t_s t_{\mathrm{sr}} t_{\mathrm{bs}}, \tag{A7}$$

$$\mathbf{M}_{33} = \mathcal{D}^{-1}[-r_{\mathrm{sr}}^* + r_{\mathrm{bs}}^{*2} + r_{\mathrm{ITM}}^* r_s^* r_{\mathrm{sr}}^* r_{\mathrm{bs}}^2 - (r_{\mathrm{ITM}}^* + r_s^* r_{\mathrm{sr}}^*) t_{\mathrm{bs}}^2 - r_{\mathrm{ITM}}^* r_s^*], \tag{A8}$$

where the denominator $\mathcal{D}$ reads

$$\mathcal{D} = 1 - r_{\mathrm{ITM}}^* r_s^* r_{\mathrm{bs}}^2 - r_{\mathrm{sr}} r_{\mathrm{bs}}^{*2} + (r_{\mathrm{ITM}}^* r_{\mathrm{sr}} + r_s^*) t_{\mathrm{bs}}^2 + r_{\mathrm{ITM}}^* r_s^* r_{\mathrm{sr}}.$$

From the above input-output relation, we can define the effective coupling among three optical modes c_a, c_b and the external continuum d. Specifically, we introduce the sloshing frequency between c_a and c_b:

$$\omega_s \equiv \frac{c|\mathbf{M}_{12}|}{2\sqrt{L_{\mathrm{arm}} L_s}}, \tag{A9}$$

and two decay rates for each mode:

$$\gamma_a \equiv \frac{c|\mathbf{M}_{13}|^2}{4L_{\mathrm{arm}}}, \qquad \gamma_b \equiv \frac{c|\mathbf{M}_{23}|^2}{4L_s}. \tag{A10}$$

In addition, the resonant frequencies for each modes can also be defined, and we have

$$\omega_a \equiv \frac{c\arg(\mathbf{M}_{11})}{2L_{\mathrm{arm}}}, \qquad \omega_b \equiv \frac{c\arg(\mathbf{M}_{22})}{2L_1}, \tag{A11}$$

with "arg" being the phase angle.

[1] G. M. Harry (LIGO Scientific Collaboration), Classical Quantum Gravity **27**, 084006 (2010).
[2] T. Accadia, F. Acernese, F. Antonucci, P. Astone, G. Ballardin, F. Barone, M. Barsuglia, A. Basti, T. S. Bauer, M. Bebronne *et al.*, Classical Quantum Gravity **28**, 114002 (2011).
[3] Y. Chen, J. Phys. B **46**, 104001 (2013).
[4] S. L. Danilishin and F. Y. Khalili, Living Rev. Relativity **15** (2012).
[5] A. Buonanno and Y. Chen, Phys. Rev. D **64**, 042006 (2001).
[6] P. Purdue and Y. Chen, Phys. Rev. D **66**, 122004 (2002).
[7] A. R. Wade, K. McKenzie, Y. Chen, D. A. Shaddock, J. H. Chow, and D. E. McClelland, Phys. Rev. D **86**, 062001 (2012).
[8] J. Gough and M. R. James, IEEE Trans. Autom. Control **54**, 2530 (2009).
[9] H. Mabuchi, Phys. Rev. A **78**, 032323 (2008).
[10] J. Kerckhoff, H. I. Nurdin, D. S. Pavlichin, and H. Mabuchi, Phys. Rev. Lett. **105**, 040502 (2010).
[11] R. Hamerly and H. Mabuchi, Phys. Rev. Lett. **109**, 173602 (2012).
[12] H. J. Kimble, Y. Levin, A. B. Matsko, K. S. Thorne, and S. P. Vyatchanin, Phys. Rev. D **65**, 022002 (2001).
[13] H. Miao, H. Yang, R. X. A Adhikari, and Y. Chen, arXiv:1305.3957.
[14] V. Braginsky and F. Khalilli, *Quantum Measurements* (Cambridge University Press, Cambridge, England, 1992).
[15] M. Wang, C. Bond, D. Brown, F. Brückner, L. Carbone, R. Palmer, and A. Freise, Phys. Rev. D **87**, 096008 (2013).
[16] A. Buonanno and Y. Chen, Phys. Rev. D **67**, 062002 (2003).
[17] J. Aasi, J. Abadie, B. P. Abbott, R. Abbott, T. D. Abbott, M. Abernathy, T. Accadia, F. Acernese *et al.* (LIGO Scientific and Virgo Collaborations), arXiv:1304.0670.
[18] P. Purdue, Phys. Rev. D **66**, 022001 (2002).